SUPPORTING INFORMATION: Effects of coherent ferroelastic domain walls on the thermal conductivity and Kapitza conductance in bismuth ferrite

Patrick E. Hopkins,[1, a)] Carolina Adamo,[2] Linghan Ye,[3] Bryan D. Huey,[4] Stephen R. Lee,[5] Darrell G. Schlom,[6] and Jon F. Ihlefeld[5, b)]

[1)]*Department of Mechanical and Aerospace Engineering, University of Virginia, Charlottesville, Virginia, USA 22904*

[2)]*Department of Materials Science and Engineering, Cornell University, Ithaca, New York 14853, USA*

[3)]*Institute of Materials Science, University of Connecticut, Storrs, Connecticut, USA 06269*

[4)]*Institute of Materials Science,University of Connecticut,Storrs, Connecticut, USA 06269*

[5)]*Sandia National Laboratories, Albuquerque, New Mexico, USA 87123*

[6)]*Department of Materials Science and Engineering, Cornell University, Ithaca, New York, USA 14853*

[a)]Electronic mail: phopkins@virginia.edu

[b)]Electronic mail: jihlefe@sandia.gov

PIEZO FORCE MICROSCOPY CHARACTERIZATION OF DOMAINS

The domain structure and domain boundaries were characterized via angle-resolved Piezo Force Microscopy (PFM) using a procedure outlined by Desmarais et al.[1] Briefly, PFM was performed with an Asylum Research MFP-3d AFM operated in contact mode with a conductive probe. An external function generator was used to bias the probe with an AC voltage causing piezo-actuation within the film that was detected with a lock-in amplifier.[2] Angle-resolved PFM was performed by exciting and recording the distinct normal and lateral piezoresponse at spectrally separate frequencies, enabling out-of-plane (z-direction) and in-plane polarizations (y-direction), respectively, to be simultaneously recorded. To identify the full in-plane variant, the specimen was then rotated by 90°, the same location was found, and a second set of normal and complementary lateral (now in the x-direction) PFM images was acquired.

Figure 1 presents $\left[\bar{1}00\right]$ lateral PFM images for both the 4-domain (a) and 2-domain (b) variant specimens, their corresponding $\left[0\bar{1}0\right]$ perpendicular lateral piezoresponse (c,d), the normal $[001]$ PFM signal (e,f) and the topography (g,h). A custom image analysis script was employed to generate maps for each specimen of domain orientations, domain boundary locations, domain boundary angles, and domain boundary types (head-to-head polarization, head-to-tail polarization, etc).

TIME DOMAIN THERMOREFLECTANCE

We measure the thermal transport properties of our samples with TDTR. TDTR is a pump-probe technique in which laser pulses emanate from a Ti:Sapphire oscillator; in our case, our laser operates at 80 MHz with pulses centered at 802 nm and pulse widths of $\sim$300 fs at the sample surface. We delay the time in which the probe pulses reach the sample with respect to the pump pulses with a mechanical delay stage that gives us $\sim$7 ns of pump-probe delay. Our pump pulses are frequency doubled to 401 nm. For this study, we modulate the pump path at 11.39 MHz with a linearly amplified sinusoid and monitor the ratio of the in-phase to out-of-phase signal of the probe beam with a lock in amplifier. Our pump and probe spots are focused to roughly 25 μm and 6 μm radii, respectively, at the sample surface. When modulating at 11.39 MHz with these spot sizes, we are negligibly sensitive to any in-plane transport in the $BiFeO_3$ films or $SrTiO_3$ substrates.[3,4] We find that five TDTR measurements on each film give us enough repeatability to report mean values

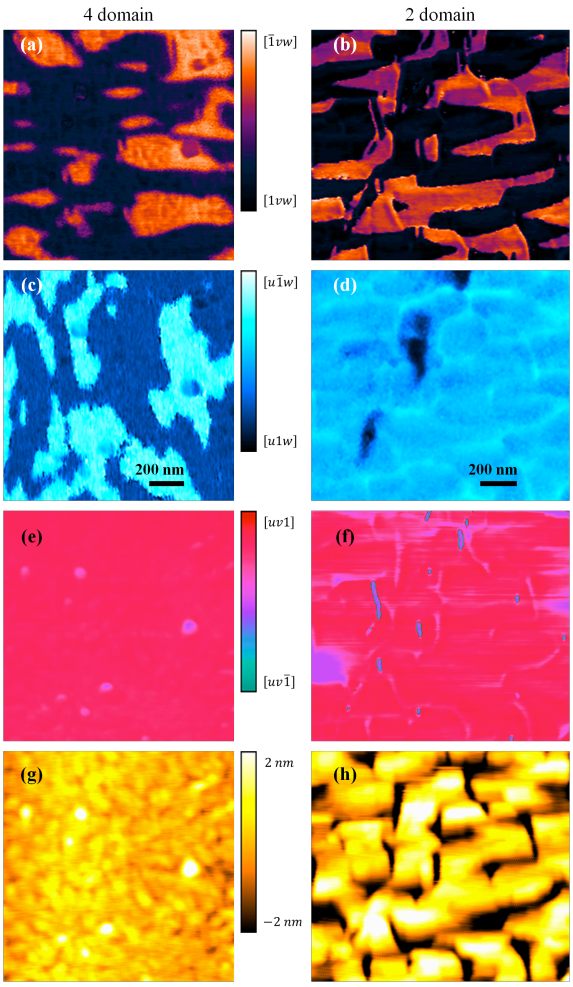

FIG. 1. Multiple piezo force microscopy images acquired at a single location for 4-domain (left) and 2-domain (right) $BiFeO_3$ thin films. Perpendicular vector components of local ferroelectric domain orientations are shown in different images. Bright contrast indicates in-plane domain polarization (a,b), perpendicular in-plane polarization (c,d), normal out-of-plane domain polarization (e,f), and topographic protrusions (g,h). The 200 nm scale bars in (c) and (d) apply to all images for each specimen (columns); contrast bars apply to each image type (rows).

and the corresponding standard deviation about the mean of the $BiFeO_3$ thermal conductance. Due to the thickness of the $BiFeO_3$ films (30 nm), we are not sensitive to the heat capacity of the $BiFeO_3$ (see Fig. 2 and accompanying discussion later in this section), and we measure the conductance across the Pt/$BiFeO_3$/$SrTiO_3$ interface $\left(h_{\mathrm{K,Pt/BiFeO_3/SrTiO_3}}\right)$. These measured conductances are shown in Fig. 3 and discussed below. The model that we use to determine this conductance from our TDTR data has been discussed in detail by several groups elsewhere.[3–5]

Prior to TDTR measurements we coat a small area (800 μm $\times$ 800 μm) of the $BiFeO_3$ films with 50 nm of Pt via RF magnetron sputtering. The thickness was verified with profilometry. We cannot measure the local film thickness of the Pt transducer via picosecond ultrasonics[6,7] since the reflectivity of Pt at 800 nm only weakly depends on strain, but we make multiple profilometry measurements on various edges of the Pt pad to ensure accurate Pt thickness and therefore minimize this uncertainty in our measurements.

As mentioned above, due to the thickness of the $BiFeO_3$ films (30 nm), we are not sensitive to the heat capacity of the $BiFeO_3$, and we measure the conductance across the Pt/$BiFeO_3$/$SrTiO_3$ interface $\left(h_{\mathrm{K,Pt/BiFeO_3/SrTiO_3}}\right)$. To show this quantitatively, we calculate the sensitivity of the TDTR signal ($-V_{\mathrm{in}}/V_{\mathrm{out}}$ - which is related to the change in temperature on the surface of the platinum) as a function of pump probe delay time. We define this sensitivity of our TDTR signal to some thermophysical property p as[8]

$$S_p = \frac{\partial \ln\left[-\frac{V_{\mathrm{in}}}{V_{\mathrm{out}}}\right]}{\partial \ln\left[p\right]}, \tag{1}$$

which we calculate with a 1% perturbation in p, so Eq. 1 reduces to[9]

$$S_p = 100\frac{V_{\mathrm{out}}\left(p\right)}{V_{\mathrm{in}}\left(p\right)}\left(\frac{V_{\mathrm{in}}\left(1.01p\right)}{V_{\mathrm{out}}\left(1.01p\right)} - \frac{V_{\mathrm{in}}\left(p\right)}{V_{\mathrm{out}}\left(p\right)}\right). \tag{2}$$

To investigate the sensitivity to the heat capacity, C, of the 30 nm $BiFeO_3$ thin film as compared to thermal conductivity, κ, of the $BiFeO_3$ film and the thermal boundary conductance, h_{K}, between the Pt transducer and the $BiFeO_3$ film, we calculate these sensitivities via 2 for a 3 layer system (50 nm Pt/30 nm $BiFeO_3$/$SrTiO_3$) at room temperature. We assume literature values for the heat capacity and thermal conductivity of the 50 nm Pt transducer ($C_{\mathrm{Pt}} = 2.85 \times 10^6$ MJ m^{-3} K^{-1} and $\kappa_{\mathrm{Pt}} = 71.6$ W m^{-1} K^{-1} (Ref.[10]) - note, we have confirmed the high quality and near bulk-like thermal conductivity of our Pt transducers via electrical resistivity measurements and the Wiedemann-Franz Law) and the $SrTiO_3$ substrate ($C_{\mathrm{SrTiO3}} = 2.81 \times 10^6$ MJ m^{-3} K^{-1} (Ref.[11]) and $\kappa_{\mathrm{SrTiO3}} = 10.1$ W m^{-1} K^{-1} (Ref.[12])). We assume a relatively high thermal boundary conductance between the $BiFeO_3$ and the $SrTiO_3$ ($h_{\mathrm{K,BiFeO3/SrTiO3}} = 1000$ MW m^{-2} K^{-1}) due to the epitaxial growth of the $BiFeO_3$ and high quality and coherency of the interface.[8] For these sensitivity calculations, we take the thermal boundary conductance between the Pt and $BiFeO_3$ as 200 MW m^{-2} K^{-1}, which is the thermal boundary conductance that we measure for Pt/$SrTiO_3$ interfaces (discussed below), the thermal conductivity of the $BiFeO_3$ as 2 W m^{-1} K^{-1}, which we

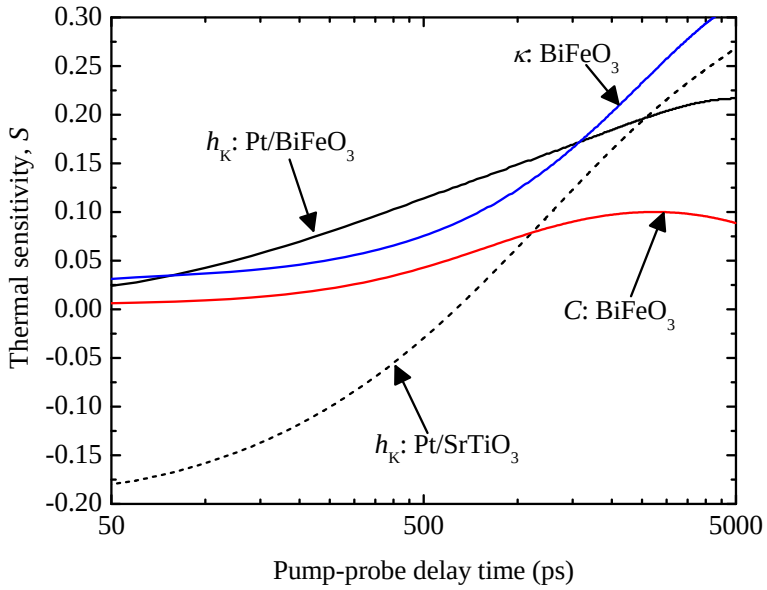

FIG. 2. TDTR sensitivity calculations based on 2 and a two- or three-layer thermal model (dashed and solids lines, respectively). Assuming a three-layer system (50 nm Pt/30 nm $BiFeO_3$/$SrTiO_3$), we have very low sensitivity to C of the $BiFeO_3$ compared to κ of $BiFeO_3$ or h_K at the Pt/$BiFeO_3$ interface. Therefore, we can treat this system as a two layer system (Pt/$SrTiO_3$) and fit h_K between the Pt films and $SrTiO_3$ substrate to determine the effective thermal conductivity of the $BiFeO_3$. Note we are extremely sensitive to h_K between the Pt films and $SrTiO_3$ using this approach, as indicated by the dashed line.

estimate from our results in the manuscript, and the heat capacity of $BiFeO_3$ as 3.1×10^6 MJ m^{-3} K^{-1} (Ref.[13]).

Our TDTR sensitivity calculations for this three layer system are shown in Fig. 2 as the solid lines. Our thermal model that we use for these sensitivity calculations has been discussed in detail elsewhere.[3–5] Note that an ideal sensitivity is very dynamic throughout the entire range of pump-probe delay times (i.e., not flat). For this three layer analysis, our TDTR measurements are always more sensitive to the thermal boundary conductance between the Pt and $BiFeO_3$ and the thermal conductivity of the $BiFeO_3$ than the heat capacity of the $BiFeO_3$. At longer time delays, we begin to become more sensitive to the $BiFeO_3$ heat capacity, but at these time delays the sensitivity to the thermal boundary conductance and thermal conductivity also increases and overwhelms the sensitivity to the heat capacity of the thin $BiFeO_3$ film. As our measurements have very low

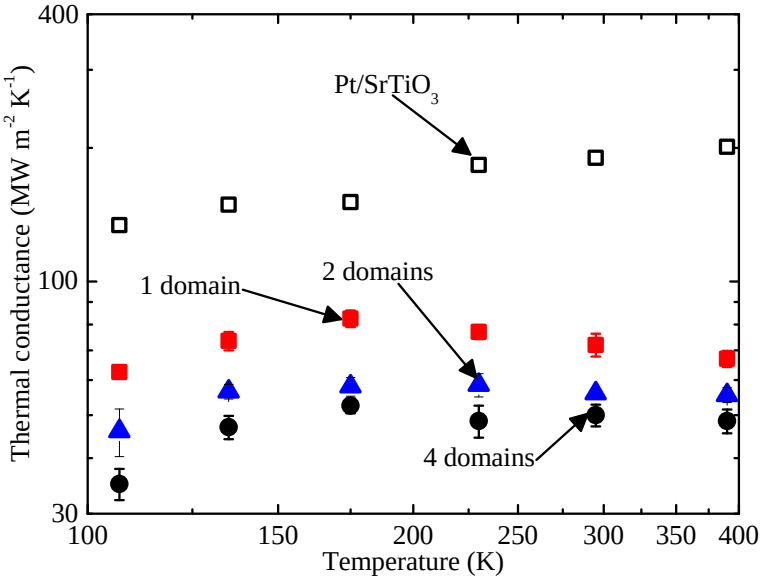

FIG. 3. Measured conductances from our TDTR data using a two-layer model. The conductances determined from the Pt/$BiFeO_3$/$SrTiO_3$ are represented by the filled symbols and the thermal boundary conductance measured from our Pt/$SrTiO_3$ calibration samples is shown by the unfilled squares. The data in Fig. 3 of the manuscript are derived by multiplying the conductance from the Pt/$BiFeO_3$/$SrTiO_3$ by the thickness of the $BiFeO_3$ (30 nm).

sensitivity to the heat capacity of the 30 nm $BiFeO_3$ films, we can treat this system as a two-layer system (Pt/$SrTiO_3$) and fit our TDTR data via the thermal boundary conductance between the Pt film and $SrTiO_3$ substrate to determine the conductance of the 30 nm $BiFeO_3$ film. As shown in Fig. 2 by the dashed line, our measurements are very sensitivity to h_{K} between the Pt and $SrTiO_3$, yielding low uncertainty.

Therefore, the values reported in this manuscript are determined from fitting our TDTR data to a two-layer model by iterating the thermal boundary conductance between the Pt transducer film and the $SrTiO_3$ substrate. These resulting conductances are shown in Fig. 3. The effective thermal conductivities of the $BiFeO_3$ films reported in Fig. 3 in the manuscript are derived by multiplying the conductances of the Pt/$BiFeO_3$/$SrTiO_3$ samples (filled symbols) by the thicknesses of the films (30 nm). Note that this conductance actually represents three thermal pathways: the thermal boundary conductance between the Pt transducer and the $BiFeO_3$ film, the thermal conductiv-

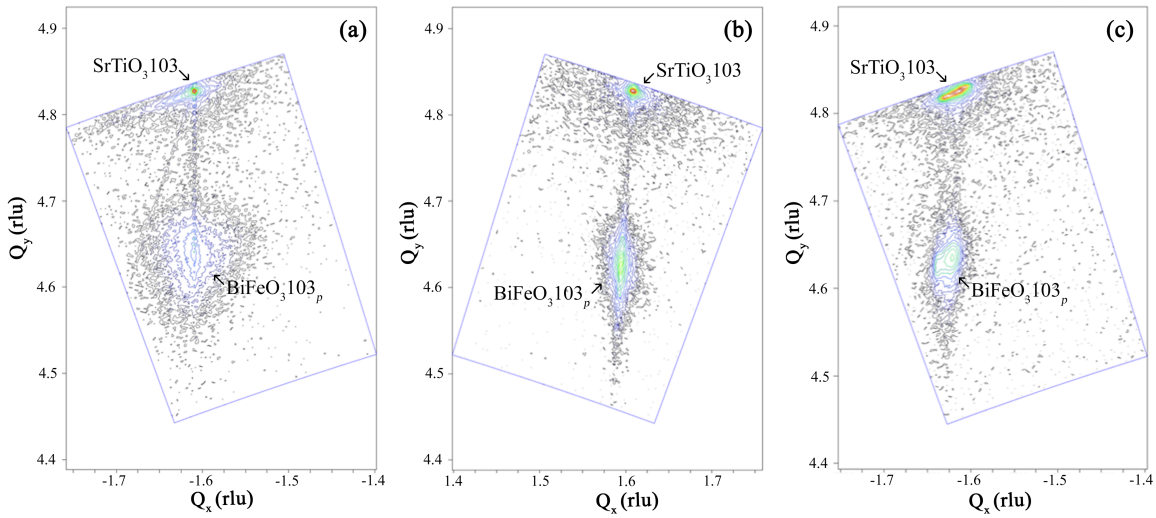

FIG. 4. Reciprocal space mapping of the 103 peaks in 30 nm thick $BiFeO_3$ films grown on (001)-oriented $SrTiO_3$ with (a) 4 domain variants, (b) 2-domain variants and (c) a single domain variant.

ity of the $BiFeO_3$ film, and the thermal boundary conductance between the $BiFeO_3$ film and the $SrTiO_3$ substrate. Due to the epitaxial growth of the $BiFeO_3$ and high quality and coherency of the interface, we are minimally sensitive to this $BiFeO_3/SrTiO_3$ conductance since the thermal boundary conductance is very high at epitaxial interfaces,[8] as we mentioned previously. To estimate the thermal boundary conductance between the Pt and $BiFeO_3$ film, we measure the thermal boundary conductance between a Pt transducer and a single crystalline $SrTiO_3$ substrate. These measurements are shown in Fig. 3 (unfilled squares), and are roughly half an order of magnitude greater than the conductance measured on the $Pt/BiFeO_3/SrTiO_3$ samples. Due to the surface quality of the $BiFeO_3$ films owing to the epitaxial growth, the $Pt/BiFeO_3$ thermal boundary conductances are most likely similar to those at the $Pt/SrTiO_3$ interfaces. Therefore, we can conclude that our conductances measured in the $Pt/BiFeO_3/SrTiO_3$ samples are primarily dominated by the thermal conductivity of the $BiFeO_3$ films, resulting in the effective thermal conductivities reported in Fig. 3 of the manuscript.

X-RAY DIFFRACTION RECIPROCAL SPACE MAPS

X-ray diffraction reciprocal space maps were measured in the proximity of the $SrTiO_3$ 103 reflection with the results shown in Fig. 4 for each of the three samples. For strain-relaxed four-

variant $BiFeO_3$ films peak splitting of the 103_p $BiFeO_3$ would be anticipated.[14] In these films, we instead observe a single 103_p diffraction peak for each of the films regardless of number of domain variants. This indicates that the films are pseudomorphically strained owing to coherent epitaxial growth on the $SrTiO_3$ substrate. The 103_p peak on the four-variant film is slightly more diffuse than that for the 2-variant or single-variant films, which may be indicative of inhomogeneous strain at the domain boundaries.

REFERENCES

[1] J. Desmarais, J. F. Ihlefeld, T. Heeg, J. Schubert, D. G. Schlom, and B. D. Huey, Applied Physics Letters **99**, 162902 (2011).

[2] B. D. Huey, R. Nath, S. Lee, and N. A. Polomoff, Journal of the American Ceramic Society **95**, 1 (2012).

[3] P. E. Hopkins, J. R. Serrano, L. M. Phinney, S. P. Kearney, T. W. Grasser, and C. T. Harris, Journal of Heat Transfer **132**, 081302 (2010).

[4] A. J. Schmidt, X. Chen, and G. Chen, Review of Scientific Instruments **79**, 114902 (2008).

[5] D. G. Cahill, Review of Scientific Instruments **75**, 5119 (2004).

[6] C. Thomsen, J. Strait, Z. Vardeny, H. J. Maris, J. Tauc, and J. J. Hauser, Physical Review Letters **53**, 989 (1984).

[7] C. Thomsen, H. T. Grahn, H. J. Maris, and J. Tauc, Physical Review B **34**, 4129 (1986).

[8] R. M. Costescu, M. A. Wall, and D. G. Cahill, Physical Review B **67**, 054302 (2003).

[9] P. E. Hopkins, L. M. Phinney, J. R. Serrano, and T. E. Beechem, Physical Review B **82**, 085307 (2010).

[10] D. E. Gray, *American Institute of Physics Handbook*, 3rd ed. (McGraw Hill, New York, 1972).

[11] S. S. Todd and R. E. Lorenson, Journal of the American Chemical Society **74**, 2043 (1952).

[12] Y. Wang, K. Fujinami, R. Zhang, C. Wan, N. Wang, Y. Ba, and K. Koumoto, Applied Physics Express **3**, 031101 (2010).

[13] S. Phapale, R. Mishra, and D. Das, Journal of Nuclear Materials **373**, 137 (2008).

[14] S. H. Baek, H. W. Jang, C. M. Folkman, Y. L. Li, B. Winchester, J. X. Zhang, Q. He, Y. H. Chu, C. T. Nelson, M. S. Rzchowski, X. Q. Pan, R. Ramesh, L. Q. Chen, and C. B. Eom, Nature Materials **9**, 309 (2010).